In-Situ Phase Mapping and Direct Observations of Phase Transformations during Arc Welding of 1045 Steel

J.W. ELMER and T.A. PALMER

In-situ spatially resolved X-ray diffraction (SRXRD) experiments were performed during gas tungsten arc (GTA) welding of AISI 1045 C-Mn steel. Ferrite (α) and austenite (γ) phases were identified and quantified in the weld heat-affected zone (HAZ) from the real time SRXRD data. The results were compiled with weld temperatures calculated using a coupled thermal fluids model to create a phase map of the HAZ. Kinetics of the $\alpha \rightarrow \gamma$ transformation during weld heating and the reverse $\gamma \rightarrow \alpha$ transformation during weld cooling were extracted from the map. Superheating as high as 250 °C above the A3 temperature was observed for the $\alpha \rightarrow \gamma$ phase transformation to reach completion at locations near the fusion zone (FZ) boundary. The SRXRD experiments revealed that the newly created γ phase exists with two distinct lattice parameters, resulting from the inhomogeneous distribution of carbon and manganese in the starting pearlitic/ferritic microstructure. During cooling, the reverse $\gamma \rightarrow \alpha$ phase transformation was shown to depend on the HAZ location. In the fine-grained region of the HAZ, the $\gamma \rightarrow \alpha$ transformation begins near the A3 temperature and ends near the A1 temperature. In this region, where the cooling rates are below 40 °C/s, the transformation occurs by nucleation and growth of pearlite. In the coarse-grained region of the HAZ, the $\gamma \rightarrow \alpha$ transformation requires 200 °C of undercooling for completion. This high degree of undercooling is caused by the large grains coupled with cooling rates in excess of 50 °C/s that result in a bainitic transformation mechanism.

I. INTRODUCTION

THE optimized base metal properties of steels are altered during welding by the severe thermal cycles imparted on the workpiece by the localized welding heat source. As a result, nonequilibrium microstructures are created in the fusion zone (FZ) and heat-affected zone (HAZ) of the weld. These microstructures differ significantly in appearance and properties from those found in the base metal.[1,2,3] Transformation from the body-centered cubic (bcc) form of iron, referred to as ferrite, and the face-centered cubic (fcc) form of iron, referred to as austenite, is principally responsible for these changes in microstructure. This transformation during the weld heating cycles has a distinct effect on the final microstructure that forms during cooling by controlling the extent of the transformation and the resulting carbon content in the austenite.[4] It is well known that carbon plays an important role in these transformations.[1,2,3] Increases in the carbon content are known to intensify the microstructural changes that occur and to increase the amount of nonequilibrium phases that are created during cooling. In order to better understand the microstructural evolution in steel welds, *in-situ* X-ray diffraction (XRD) studies are being performed to directly observe the phase transformations that occur during welding of low and medium carbon steels.

Time-resolved X-ray diffraction (TRXRD) has recently been used to investigate phase transformations that occurred during stationary gas tungsten arc (GTA) spot welding of both medium carbon (AISI 1045)[5] and low-carbon (AISI 1005) steels.[6] These real-time synchrotron-based experiments tracked the phases present at discreet time resolutions, on the order of 100 ms, in the HAZ of welds under rapid heating and cooling rates, typically in excess of 100 °C/s. The relative fractions of α and γ phases present at each time increment were then measured during both weld heating and cooling. Modeling of the TRXRD spot welds was performed using a transient three-dimensional (3-D) coupled thermal fluids code to determine the time-temperature profile of the welds.[7] Differences in austenitization rates of the low and high-carbon steels were observed and were attributed to differences in amounts and distributions of the pearlite and allotriomorphic ferrite phases in the base metal microstructures.[5]

Spatially resolved X-ray diffraction (SRXRD) has also been used to investigate phase transformations in the low-carbon 1005 C-Mn steel.[8–13] From these data, a map showing the locations of the γ and α phases present across the width of the HAZ in a typical arc weld was created.[8,9] Kinetic modeling of the data presented in the $\alpha \rightarrow \gamma$ phase transformation map was performed using a Johnson–Mehl–Avrami (JMA) approach in order to determine JMA kinetic parameters for the 1005 steel under real welding conditions.[10–13] Using this kinetic description of the $\alpha \rightarrow \gamma$ phase transformation and other phase transformation models, time-temperature-transformation (TTT) and continuous-heating-transformation (CHT) diagrams were constructed and were used to predict microstructure evolution.[9]

The SRXRD technique was further used to determine the influence of weld heat input on the width of the $\alpha + \gamma$ and γ phase regions in the HAZ of the 1045 steel.[14,15] These experiments revealed that the γ phase in the 1045 steel exists with two distinct lattice parameters. The presence of these different lattice parameters results in a distinct splitting of the γ peaks at temperatures above the A3 temperature. The split peaks eventually combined into one diffraction peak at elevated temperatures as diffusion of C and Mn homogenized the microstructure at HAZ temperatures near the solidus temperature of the alloy.

J.W. ELMER, Deputy Program Element Leader, and T.A. PALMER, Metallurgist, are with the Lawrence Livermore National Laboratory, Livermore, CA 94550. Contact e-mail: palmer18@llnl.gov

Manuscript submitted September 22, 2005.

In this investigation, the medium carbon steel containing 0.46 wt pct C was investigated using the SRXRD technique in order to create a complete map of the phases that exist in the HAZ during welding. This map is similar to the map previously created for the low-carbon steel weld[8,9] and provides a means to compare the kinetics of the $\alpha \rightarrow \gamma$ phase transformation in steels with two different carbon contents (0.05 and 0.46 wt pct C). Quantitative information about the phase transformation kinetics was extracted from these data through thermal and phase transformation modeling. The results presented here demonstrate the differences in the phase transformation behavior between low and medium carbon steels and show how *in-situ* XRD can be used to provide real time observations of important phase transformations during the welding of steels.

II. EXPERIMENTAL PROCEDURES

A. *SRXRD Experiments*

Gas tungsten arc welds were made on AISI 1045 steel cylindrical forged bar samples (0.46C, 0.85Mn, 0.27Si, 0.02Ni, 0.11Cr, 0.014P, 0.01Cu, 0.02S, 0.027Al, 0.001Nb, 0.01Mo, 0.005V; by wt pct). These samples were machined from 10.8-cm-diameter forged bar stock into welding samples, 12.7-cm long and 10.2 cm in diameter. Welds were then made on the cylindrical steel bars in an environmentally sealed chamber to avoid atmospheric contamination of the weld. During welding, the synchrotron beam was used to map the phases in the weld HAZ. A schematic illustration of the experimental setup is shown in Figure 1(a), and a brief summary of the welding parameters is given in Table I. Additional details of similar welding experiments are reported elsewhere.[8,9,15] Figure 1(b) shows a schematic diagram of the weld region, with the *X*-*Y* spatial coordinates used for mapping marks, indicating that the X-ray data are taken along the *Y* direction, which is perpendicular to the welding direction.

The *in-situ* SRXRD experiments were performed during welding using the 31-pole wiggler Beam Line 10-2 at the Stanford Synchrotron Radiation Laboratory with a Stanford positron-electron accumulation ring operating at an electron energy of 3.0 GeV and an injection current of approximately 100 mA. Figure 1 illustrates the SRXRD setup, in which the focused monochromatic synchrotron X-ray beam is passed through a 260-μm tungsten pinhole to render a submillimeter beam on the sample at an incident angle of ~25 deg. This arrangement yields a beam flux on the sample of $\sim 10^{11}$ photons/s, which was measured experimentally using an ion chamber immediately downstream from the pinhole. A photon energy of 12.0 keV ($\lambda = 0.1033$ nm) was chosen for these experiments, because this energy is far enough above the Fe K-edge (7.112 keV) to minimize the background contribution due to Fe K-fluorescence from the steel sample. The background radiation was further reduced using a thin Nb foil (25 μm), which was placed directly in front of the detector to act as a filter.

X-ray diffraction patterns were recorded using a 50-mm long 2048 element position sensitive Si photodiode array detector. The array was mounted on a dual-stage water-cooled Peltier effect thermoelectric cooler at a distance of approximately 10 cm behind the weld to cover a 2θ range from 22 to 52 deg. This 2θ range was optimized to contain a total of six diffraction peaks, three from the α phase and three from the γ phase, as indicated in the calculated XRD pattern for iron in Figure 2. Calibration of the 2θ locations of the XRD patterns

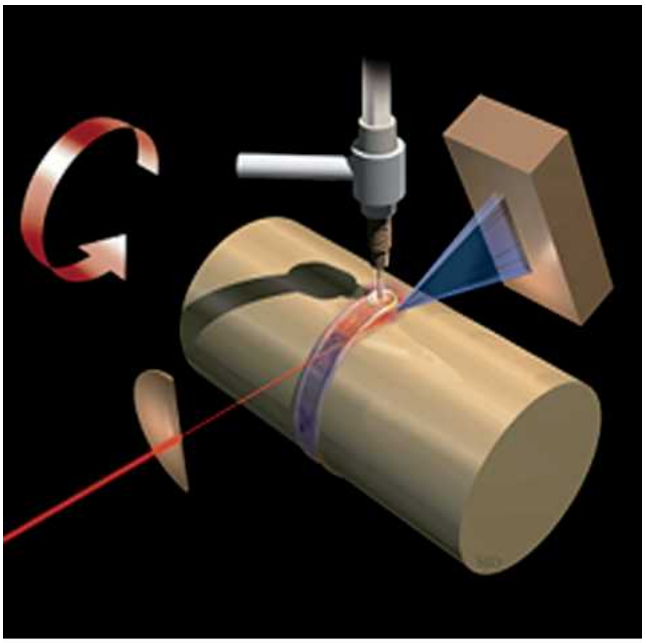

(*a*)

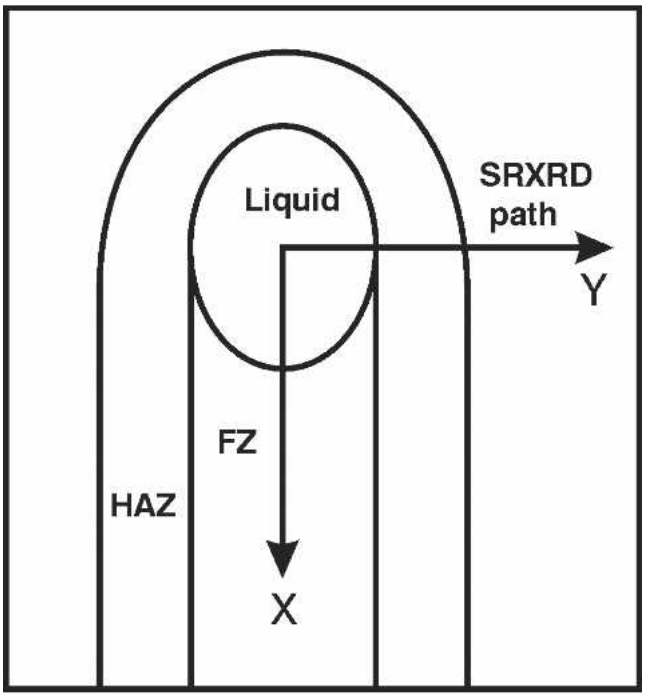

(*b*)

Fig. 1—(*a*) Schematic diagram of the SRXRD experimental setup for synchrotron-based *in-situ* observations of phase transformations during welding. Shown are the X-ray beam passing through the pinhole, the direction of rotation of the bar beneath the fixed welding torch, and the X-ray detector downstream from the weld. (*b*) Schematic drawing of the quasi-steady-state weld region showing the coordinate system used throughout the article.

Table I. Summary of GTA Welding Parameters Used in the SRXRD experiments

Welding electrode	W-2 pct Th
Electrode diameter (mm)	4.7
Torch polarity	DCEN
Maximum current (A)	175
Background current (A)	123
Pulsing frequency (Hz)	300
Peak on time (pct)	50
Arc voltage (V)	16.2
Weld speed (mm/s)	0.6
Shielding gas	helium
Resulting fusion zone width (mm)	10.0
Resulting fusion zone depth (mm)	5.6

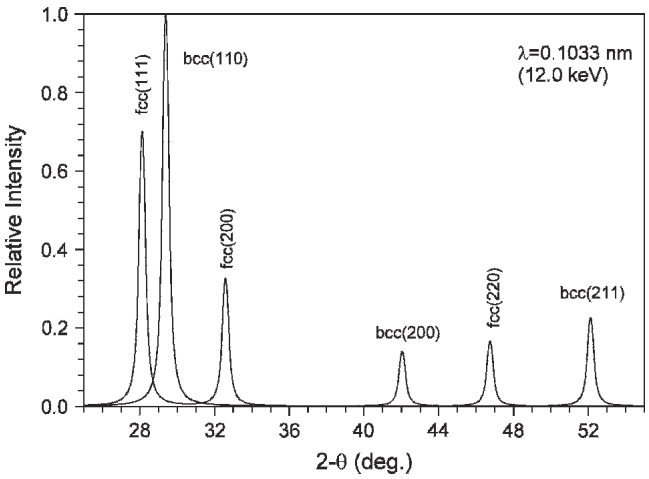

Fig. 2—Calculated diffraction pattern of iron, showing the three possible peaks for each phase that can appear in the detector window. Equal amounts of the fcc and bcc phases are assumed.

was performed using a thin niobium foil that has a well-characterized bcc crystal structure. This foil was placed directly on the bar to be welded, allowing an initial diffraction pattern to be taken of it just prior to initiating the weld.

B. *Diffraction Patterns Were Taken during Welding by Jogging the Weld Sample with Respect to the Stationary X-ray Beam in 0.2-mm Steps Perpendicular to the Welding Direction*

In each SRXRD run, approximately 100 diffraction patterns were gathered along a linear path beginning at a unique *x*-axis location on the centerline of the weld and proceeding outward through the weld HAZ. Overall, a distance of approximately 20 mm from the weld centerline was examined. Each data point consisted of a diffraction pattern recorded during a 4-second integration time while the beam was at a fixed location and the bar was rotating under the torch at a constant speed. With the weld travel speed of 0.6 mm/s, each SRXRD pattern was integrated over a distance of approximately 2.4 mm on the surface of the bar.

Postweld analysis of each peak in every diffraction pattern was performed to determine the semiquantitative volume fractions of γ and α present as a function of welding time. This analysis measured the integrated intensity of each peak using a sum of one or more Gaussian peak profile

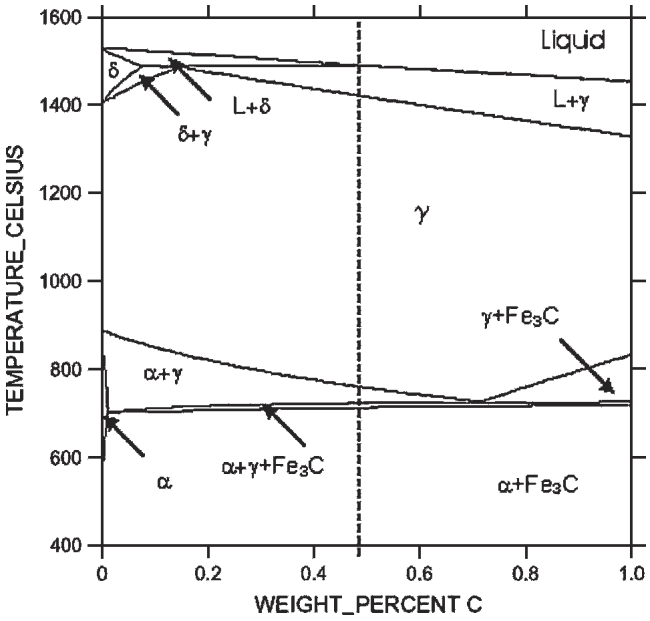

Fig. 3—Calculated pseudo-binary phase diagram for the AISI 1045 steel. The nominal carbon concentration of the alloy is indicated as the vertical dashed line.

fitting functions using an automated curve-fitting routine developed in IGOR PRO,* version 4.0.[16] The raw integrated intensities of the diffraction peaks were then converted into phase fractions using a structure factor approach, as described in more detail elsewhere.[9]

*IGORPRO is a trademark of Wave Metrics, Inc., Portland, OR.

C. *Phase Equilibria and Base Metal Microstructure*

The phase transformation sequence of the 1045 steel was calculated from thermodynamic relationships using THERMO-CALC,* version 2 for Windows, and the TCFE2 database.[17] These calculations were used to determine the transformation temperatures for the AISI 1045 steel by considering the effects of Fe, C, Si, Mn, Ni, and Cr on the stability of the liquid, ferrite, austenite, and cementite phases. The calculated phase transformation temperatures for this multicomponent alloy are illustrated in the pseudo-binary diagram shown in Figure 3, where the vertical dashed line indicates the nominal carbon content of the alloy.

*THERMO-CALC is a trademark of Thermo-Calc Software, Inc., Stockholm, Sweden.

The thermodynamic calculations indicate that the equilibrium starting microstructure of this alloy will consist of a mixture of α and Fe_3C carbide phases. During heating, this microstructure will begin to transform to γ at a calculated A1 temperature of 712 °C, while complete transformation will occur at a calculated A3 temperature of 765 °C. The γ that forms will remain stable until melting begins to occur at a calculated solidus temperature of 1410 °C. Note that δ ferrite does not form in this alloy, because the δ ferrite field only exists at carbon contents lower than 0.45 pct in this

steel. The sequence of transformations during heating is reversed during cooling. However, kinetic limitations may alter the predicted phase transformation start and completion temperatures and produce nonequilibrium phases.

The starting microstructure of the 1045 steel is shown in Figure 4(a), as revealed by polishing the base meal and etching in a 2 pct nital (nitric acid and alcohol) solution. This microstructure contains allotriomorphic ferrite, which is the light etching phase that outlines the prior γ grain boundaries. Inside the prior γ grains, the microstructure consists of pearlite colonies that etch dark and occupy the majority of the microstructure. A higher magnification micrograph highlighting the lamellar structure of the pearlite is shown in Figure 4(b). Quantitative metallography was performed on this microstructure using IMAGE-PRO,* version 4.1. Measurements of the area fraction of allotriomorphic ferrite made at several locations indicate that the microstructure contains 12 pct allotriomorphic ferrite and 88 pct pearlite. The prior γ grain size of the base metal was measured to be 92.8 μm in diameter. In addition, the size of the allotriomorphic grain boundary α phase was shown to be 15- to 20-μm wide, with some patches reaching 30 μm or more in places.

*IMAGEPRO is a trademark of Media Cybernetics, Inc., Silver Springs, MD.

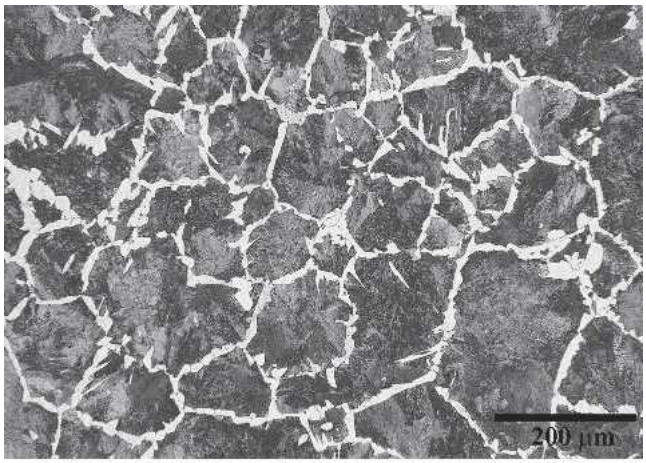

(*a*)

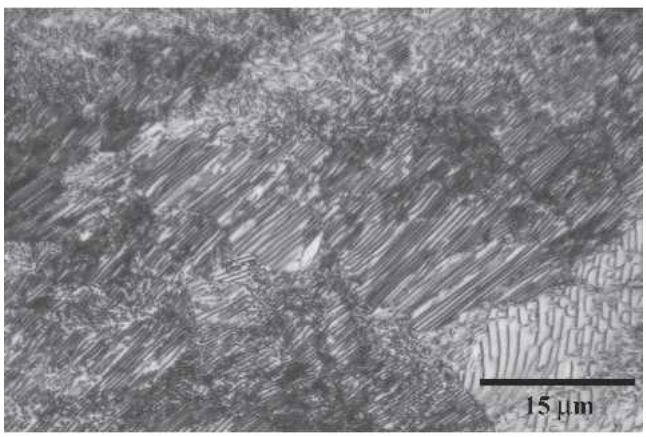

(*b*)

Fig. 4—(*a*) Base metal microstructure showing allotrimorphic ferrite outlining the prior austenite grains and pearlite colonies inside the grains. (*b*) High-magnification optical micrograph showing the lamellar microstructure typical of the pearlite colonies within the grains.

D. *Coupled Thermal-Fluid Numerical Modeling of Weld Temperatures*

The SRXRD experimental results provide information about phase transformations as a function of location around the weld but none concerning weld temperatures. Since these transient weld temperatures are difficult to measure accurately, an alternative means for determining the temperatures at locations surrounding the weld pool must be applied. In order to relate weld location to weld temperature, a numerical model was used. The weld model employed here is a well-tested 3-D numerical heat transfer and fluid flow model, which is described in more detail in References 18 and 19 and has been applied to similar SRXRD welding experiments, as discussed elsewhere.[11,12]

The thermal calculations were made under quasi-steady-state conditions in a fixed Cartesian coordinate system attached to and moving with the heat source. Since the weld pool displays a mirror symmetry, calculations were performed on only half the workpiece, and a flat weld pool surface is assumed. The electromagnetic, surface tension gradient, and buoyancy driving forces present in the transient weld pool convection were taken into account during these calculations. A computational domain of $76 \times 43 \times 44$ grid points encompassing a volume having dimensions of 410-mm length, 2-mm width, and 23-mm depth was used. Nonuniform grid spacing, with finer grids located near the heat source, where the temperature gradients were the highest, was also used for maximum resolution of the variables. The boundary conditions used in these calculations are similar to those used in previous studies.[14,15] The thermophysical properties used to represent the 1045 steel alloy in these calculations are given in Table II.[20,21] The calculated weld pool dimensions and selected isotherms were then compared with the experimental weld pool dimensions and to the location corresponding to the first appearance of γ in the SRXRD results. The cross-sectional shape of the calculated weld pool at its maximum size matched the experimental weld cross section, which has a width just under 10 mm and a depth of 5.7 mm.

In addition to calculating the temperature distribution around the weld, the model was used to calculate the temperature profiles and the heating/cooling rates at specific HAZ locations. Figure 5 plots the results of these calculations where the temperature profiles were taken at different distances parallel to the welding direction. This figure shows how the distance from the weld centerline influences the peak temperatures and overall thermal cycles of the weld. The HAZ can be approximated as the region between the melting point of the steel at the $Y = 5.0$ mm location, and the A1 temperature, which has its peak near the $Y = 10$ mm location. Within this region, the range of heating rates at the A1 temperature for this weld were calculated to vary from approximately 80 °C/s near the fusion line to 25 °C/s near the edge of the HAZ, whereas the cooling rates are

smaller and vary from 60 °C/s near the fusion line to 10 °C/s near the edge of the HAZ.

These temperatures are also compared with the phase transformation temperatures predicted from thermodynamics (Figure 3) and will be used later to calculate heating and cooling rates in the HAZ as well as the peak temperatures experienced in different portions of the HAZ. The important isotherms for the 1045 steel are the A1 (712 °C), where the microstructure begins to transform to γ on heating; the A3 (765 °C), where complete transformation to γ will occur on heating; and the melting point of 1410 °C. During cooling, these same isotherms are important, plus two additional ones representing the bainite start (485 °C) and the martensite start temperatures (324 °C).[5]

Table II. Summary of Material and Modeling Parameters Used in Heat Transfer Modeling of Weld Pool Size and Shape[20,21]

Material Parameters	Value
Density of liquid (gm/cm^3)	7.87
Effective viscosity of liquid (gm/cms)	0.75
Solidus temperature (K)	1694
Liquids temperature (K)	1767
Enthalpy of solid at melting point (cal/g)	251
Enthalpy of liquid at melting point (cal/g)	315.5
Specific heat of solid (cal/g K)	0.095
Specific heat of liquid (cal/g K)	0.3
Thermal conductivity of solid (cal/cm s K)	0.1
Effective thermal conductivity of liquid (cal/cm s K)	0.215
Coefficient of thermal expansion (1/K)	1.0×10^{-5}
d(gamma)/dT of pure material (dynes/cm K)	−0.155
Concentration of surface active species (wt pct)	0.020
Surface excess at saturation (mole/cm^2)	1.3×10^{-9}
Enthalpy of segregation (cal/mole)	-3.97×10^4
Entropy factor	3.2×10^{-3}
Weld Parameters	
Arc efficiency	0.85
Arc radius (mm)	0.295
Preheat temperature (°C)	200

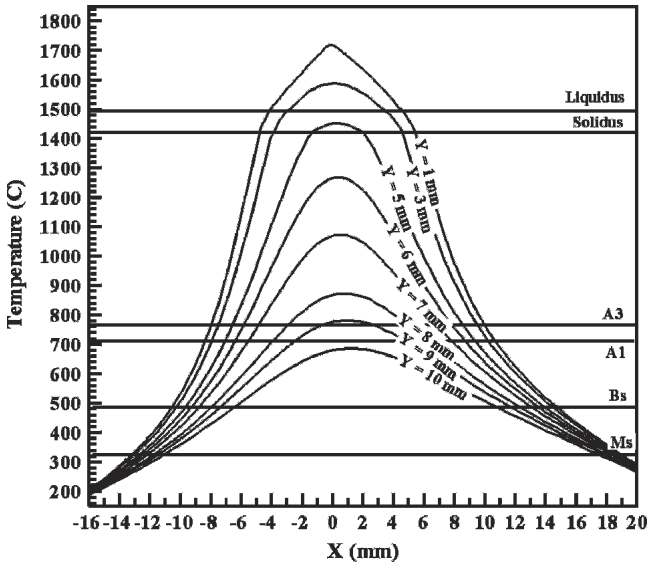

Fig. 5—Calculated heating and cooling rates through the HAZ for different distances from the centerline of the weld. Phase transformation temperatures are indicated by the horizontal lines.

III. RESULTS AND DISCUSSION

A. *SRXRD Semiquantitative Phase Map*

The SRXRD experimental data were first used to identify the spatial distribution of the α and γ phases in the weld HAZ. Each diffraction pattern was further analyzed to determine the amount of α and γ at each discreet location in the HAZ. The final results are given in Table III, which gives the relative fraction of γ for the leading (heating) side of the weld for each of the SRXRD runs. In this table, the fraction γ is given at each SRXRD location starting at the weld centerline ($Y = 0$) and moving out through the HAZ to a position in the base metal at approximately $Y = 10$ mm. Twelve different SRXRD runs are included for the heating side of the weld, starting at a location far enough ahead of the weld that no transformation was observed ($X = -9$ mm) to the position furthest from the centerline of the weld ($X = 2$ mm) where austenite was observed. Since the temperatures are highest near the centerline of the weld, the formation of austenite at these locations is either complete or nearly so. At further distances from the weld centerline, α begins to coexist with γ in increasing proportions. A α/γ coexistence region is found in a band around the weld that is between 1- and 1.6-mm wide. Only α is observed outside this α/γ coexistence band.

Table IV summarizes the relative γ fractions for the trailing (cooling) side of the weld. In this table, the γ fraction is again given at each SRXRD location starting at the weld centerline ($Y = 0$) and moving out through the HAZ to a position of $Y = 10$ mm. Thirteen additional SRXRD paths are shown, starting at the $X = 3$ mm position and moving back to the $X = 15$ mm position. The region of coexistence between γ and α moves closer to the weld centerline as the $\gamma \rightarrow \alpha$ phase transformation occurs during cooling. Additional SRXRD data were obtained at the $X = 24$ mm location, where primarily α is observed in the HAZ. These data are not shown in this table. Additional data from the resolidified portion of the weld ($Y < 5.0$ mm) are not reliable due to surface roughness that interferes with the X-ray beam and are not reported here.

A phase map showing the γ phase fractions measured across the width of the weld HAZ was developed using these SRXRD measurements. This map is shown in Figure 6 with weld isotherms, calculated using the coupled thermal fluids weld model discussed previously, superimposed over the SRXRD data. The locations of the α and γ phases are plotted with a 0.2-mm precision perpendicular to the welding direction and a 0.5-mm precision parallel to the welding direction. In the plot, the shading indicates the γ fraction, which varies from 0 pct γ (blue) to 100 pct γ (red). No δ ferrite was observed at the fusion line, which is consistent with the phase diagram shown in Figure 3. The individual SRXRD line scans were made perpendicular to the welding direction and show a variation in γ from 0 to

Table III. Semi-Quantitative Analysis Showing the Austenite Fraction at Each of the SRXRD Locations on the Heating Side of the Weld ($X < 3$ mm)

	$X = -9.0$	−8.0	−7.0	−6.0	−5.0	−4.0	−3.0	−2.0	−1.0	0.0	1.0	2.0
$Y = 0$	0.0	0.0	4.1	100.0	100.0							
0.2	0.0	0.0	17.2	100.0	100.0							
0.4	0.0	0.0	34.6	100.0	100.0							
0.6	0.0	0.0	28.4	100.0	100.0							
0.8	0.0	0.0	29.7	100.0	100.0							
1.0	0.0	0.0	20.7	100.0	100.0							
1.2	0.0	0.0	24.0	100.0	100.0							
1.4	0.0	0.0	23.8	100.0	100.0							
1.6	0.0	0.0	15.0	100.0	100.0							
1.8	0.0	0.0	14.3	100.0	100.0							
2.0	0.0	0.0	6.7	100.0	100.0							
2.2	0.0	0.0	7.9	92.1	100.0							
2.4	0.0	0.0	0.0	96.7	100.0							
2.6	0.0	0.0	0.0	95.7	100.0	100.0						
2.8	0.0	0.0	0.0	89.9	100.0	100.0						
3.0	0.0	0.0	0.0	93.0	100.0	100.0						
3.2	0.0	0.0	0.0	79.3	100.0	100.0						
3.4	0.0	0.0	0.0	67.1	100.0	100.0	100.0					
3.6	0.0	0.0	0.0	37.0	100.0	100.0	100.0					
3.8	0.0	0.0	0.0	11.1	100.0	100.0	100.0					
4.0	0.0	0.0	0.0	2.1	100.0	100.0	100.0					
4.2	0.0	0.0	0.0	0.6	100.0	100.0	100.0					
4.4	0.0	0.0	0.0	10.4	100.0	100.0	100.0					
4.6	0.0	0.0	0.0	7.2	100.0	100.0	100.0	100.0				
4.8	0.0	0.0	0.0	0.0	94.3	100.0	100.0	100.0				
5.0	0.0	0.0	0.0	0.0	83.0	100.0	100.0	100.0				
5.2	0.0	0.0	0.0	0.0	64.8	100.0	100.0	100.0		100.0	100.0	100.0
5.4	0.0	0.0	0.0	0.0	64.3	100.0	100.0	100.0	100.0	100.0	100.0	100.0
5.6	0.0	0.0	0.0	0.0	37.6	100.0	100.0	100.0	100.0	100.0	100.0	100.0
5.8	0.0	0.0	0.0	0.0	2.0	100.0	100.0	100.0	100.0	100.0	100.0	100.0
6.0	0.0	0.0	0.0	0.0	5.3	96.1	100.0	100.0	100.0	100.0	100.0	100.0
6.2	0.0	0.0	0.0	0.0	3.9	89.5	100.0	100.0	100.0	100.0	100.0	100.0
6.4	0.0	0.0	0.0	0.0	3.9	57.5	100.0	100.0	100.0	100.0	100.0	100.0
6.6	0.0	0.0	0.0	0.0	0.0	31.4	100.0	100.0	100.0	100.0	100.0	100.0
6.8	0.0	0.0	0.0	0.0	0.0	6.6	100.0	100.0	100.0	100.0	100.0	100.0
7.0	0.0	0.0	0.0	0.0	0.0	0.0	100.0	100.0	100.0	100.0	100.0	100.0
7.2	0.0	0.0	0.0	0.0	0.0	0.0	100.0	100.0	100.0	100.0	100.0	100.0
7.4	0.0	0.0	0.0	0.0	0.0	0.0	100.0	100.0	100.0	100.0	100.0	100.0
7.6	0.0	0.0	0.0	0.0	0.0	0.0	100.0	100.0	100.0	100.0	100.0	100.0
7.8	0.0	0.0	0.0	0.0	0.0	0.0	98.1	100.0	100.0	100.0	100.0	100.0
8.0	0.0	0.0	0.0	0.0	0.0	0.0	90.2	98.2	100.0	100.0	100.0	100.0
8.2	0.0	0.0	0.0	0.0	0.0	0.0	83.8	88.1	100.0	100.0	100.0	100.0
8.4	0.0	0.0	0.0	0.0	0.0	0.0	73.9	58.9	99.8	100.0	100.0	100.0
8.6	0.0	0.0	0.0	0.0	0.0	0.0	33.3	21.6	97.8	99.0	100.0	100.0
8.8	0.0	0.0	0.0	0.0	0.0	0.0	17.8	6.6	88.0	91.4	100.0	100.0
9.0	0.0	0.0	0.0	0.0	0.0	0.0	7.3	0.6	48.3	92.8	91.1	99.8
9.2	0.0	0.0	0.0	0.0	0.0	0.0	2.9	1.2	21.0	68.4	92.0	99.8
9.4	0.0	0.0	0.0	0.0	0.0	0.0	0.0	0.0	6.9	50.4	90.0	88.9
9.6	0.0	0.0	0.0	0.0	0.0	0.0	0.0	0.0	0.0	18.3	71.3	63.8
9.8	0.0	0.0	0.0	0.0	0.0	0.0	0.0	0.0	0.0	2.9	34.6	29.3
10.0	0.0	0.0	0.0	0.0	0.0	0.0	0.0	0.0	0.0	0.0	19.1	4.8
10.2	0.0	0.0	0.0	0.0	0.0	0.0	0.0	0.0	0.0	0.0	7.1	0.0
10.4	0.0	0.0	0.0	0.0	0.0	0.0	0.0	0.0	0.0	0.0		

100 pct over a narrow region approximately 1.0- to 1.6-mm wide. These regions indicate where the $\alpha \rightarrow \gamma$ phase transformation is taking place in the weld HAZ.

It is clear from this figure that a large γ phase field surrounds the weld pool, and that this phase field is expanded on the trailing side of the weld as compared to the A3 isotherm at 765 °C. It is apparent from the location of the γ phase field with respect to the A3 isotherm that the completion of the $\alpha \rightarrow \gamma$ phase transformation is shifted to higher temperatures on heating and to lower temperatures on cooling relative to the A3 temperature. It is also apparent that the γ phase field on the trailing side of the weld has a shape dissimilar to that of the A3 isotherm, whereby the γ region extends much further behind the isotherm in

Table IV. Semi-Quantitative Analysis Showing the Austenite Fraction at Each of the SRXRD Locations on the Cooling Side of the Weld for $3 < X < 15$ mm

	X = 3.0	4.0	5.0	6.0	7.0	8.0	9.0	10.0	11.0	12.0	13.0	14.0	15.0
Y = 0.0													
5.0	100	100.0	100.0	100.0	100.0	100.0	100.0	100.0	100.0	100.0	100.0	100.0	39.6
5.2	100	100.0	100.0	100.0	100.0	100.0	100.0	100.0	100.0	100.0	100.0	100.0	6.2
5.4	100	100.0	100.0	100.0	100.0	100.0	100.0	100.0	100.0	100.0	100.0	39.8	10.0
5.6	100	100.0	100.0	100.0	100.0	100.0	100.0	100.0	100.0	100.0	99.7	69.6	2.4
5.8	100	100.0	100.0	100.0	100.0	100.0	100.0	100.0	100.0	100.0	86.2	31.1	1.0
6.0	100	100.0	100.0	100.0	100.0	100.0	100.0	100.0	100.0	99.8	76.3	5.2	0.2
6.2	100	100.0	100.0	100.0	100.0	100.0	100.0	100.0	100.0	96.5	52.1	2.4	0.0
6.4	100	100.0	100.0	100.0	100.0	100.0	100.0	100.0	100.0	80.7	27.9	0.5	0.0
6.6	100	100.0	100.0	100.0	100.0	100.0	100.0	100.0	100.0	62.6	12.1	0.1	0.0
6.8	100	100.0	100.0	100.0	100.0	100.0	100.0	100.0	100.0	26.3	0.0	0.0	0.0
7.0	100	100.0	100.0	100.0	100.0	100.0	100.0	100.0	100.0	17.2	0.0	0.0	0.0
7.2	100	100.0	100.0	100.0	100.0	100.0	100.0	100.0	96.3	2.4	0.0	0.0	0.0
7.4	100	100.0	100.0	100.0	99.9	100.0	99.8	100.0	97.3	0.1	0.0	0.0	0.0
7.6	100	100.0	100.0	100.0	89.2	100.0	99.2	99.3	90.3	0.0	0.0	0.0	0.0
7.8	100	100.0	100.0	100.0	89.5	99.9	92.8	72.7	80.2	0.0	0.0	0.0	0.0
8.0	100	100.0	100.0	100.0	59.2	89.1	68.8	74.2	64.1	0.0	0.0	0.0	0.0
8.2	100	99.8	95.1	100.0	27.7	75.5	36.1	39.4	39.5	0.0	0.0	0.0	0.0
8.4	99.9	92.5	94.0	100.0	12.8	51.9	18.5	33.3	18.0	0.0	0.0	0.0	0.0
8.6	88.7	77.7	80.5	93.8	0.7	34.6	6.0	22.8	1.2	0.0	0.0	0.0	0.0
8.8	61.1	45.4	47.9	74.8	0.0	17.4	0.9	19.4	0.0	0.0	0.0	0.0	0.0
9.0	27.3	12.4	34.6	53.3	0.0	9.1	0.0	8.5	0.0	0.0	0.0	0.0	0.0
9.2	6.6	6.2	33.7	19.6	0.0	0.0	0.0	0.0	0.0	0.0	0.0	0.0	0.0
9.4	0.0	0.2	0.5	1.1	0.0	0.0	0.0	0.0	0.0	0.0	0.0	0.0	0.0
9.6		0.2	0.0	0.0	0.0	0.0	0.0	0.0	0.0	0.0	0.0	0.0	0.0
9.8		0.0	0.0	0.0	0.0	0.0	0.0	0.0	0.0	0.0	0.0	0.0	0.0

the region close to the fusion line ($5 < Y < 7$ mm) than it does further out from the fusion line.

Differences between the measured and calculated location of the γ phase field is evidence of the nonequilibrium conditions that exist during welding. The results indicate that some degree of superheat is required to completely transform the microstructure to γ on heating, and some degree of undercooling is required to initiate the transformation to α on cooling. In general, the lag required to complete the transformation to γ on heating follows the A3 isotherm, but is displaced further from the A3 isotherm at locations closer to the weld centerline where the heating rates are the highest. This suggests that the amount of superheating required for the $\alpha \rightarrow \gamma$ transformation varies with heating rate. The behavior on the cooling side of the weld is a bit different, whereby the region closest to the FZ requires considerable undercooling prior to measurable amounts of transformation to α being measured as compared to locations further from the fusion line that transforms close to the A3 isotherm.

B. *The* $\alpha \rightarrow \gamma$ *Phase Transformation on Heating*

In the SRXRD experiments performed here, the $\alpha \rightarrow \gamma$ transformation was experimentally measured for weld heating rates that were calculated to vary between 25 °C/s and 80 °C/s. These data can be compared to the $\alpha \rightarrow \gamma$ transformation rates for the same steel at higher heating rates of the TRXRD experiments,[5] and also for the low-carbon 1005 steel under similar heating conditions of previous SRXRD experiments.[8,9]

In the phase map shown in Figure 6, the regions of the weld that are most useful for gaining a better understanding of the progression of the $\alpha \rightarrow \gamma$ transformation during heating are the regions where both the α and γ phases coexist. This coexistence region was observed for the 1045 steel to occur between $X = -6$ mm and $X = 2$ mm, and the change in γ fraction as a function of distance from the weld centerline is plotted in Figure 7 for each of these SRXRD scan positions. A best fit line is drawn through each set of SRXRD data using a four-parameter sigmoidal relationship of the form

$$\gamma = \gamma_o + a(1 + \exp(-(y - y_o)/b))^{-1} \quad [1]$$

In this expression, γ_o, a, y_o, and b are the parameters being fit, while γ represents the measured fraction of γ at a given distance from the weld centerline. The two parameters that control the position and shape of the transformation curve are y_o and b, while a and γ_o represent the base line γ values of approximately 0 and 100 pct, respectively. The y_o parameter gives the y-axis distance from the centerline of the weld where the transformation is 50 pct complete, while b represents the rate at which the transformation takes place. Table V further summarizes the fit parameters y_o and b for the heating side of the weld. Note that the physical significance of the sigmoidal curve cannot easily be extracted from these data, because the time/temperature history leading up to each of the points along the path is different. However, the sigmoidal shape does fit the data well and represents a convenient analytical method to summarize the large amount of data presented in the map.

During heating, the $\alpha \rightarrow \gamma$ transformation curves move outward to larger Y values because of the increasing temperature, which is indicated by the increasing value of y_o.

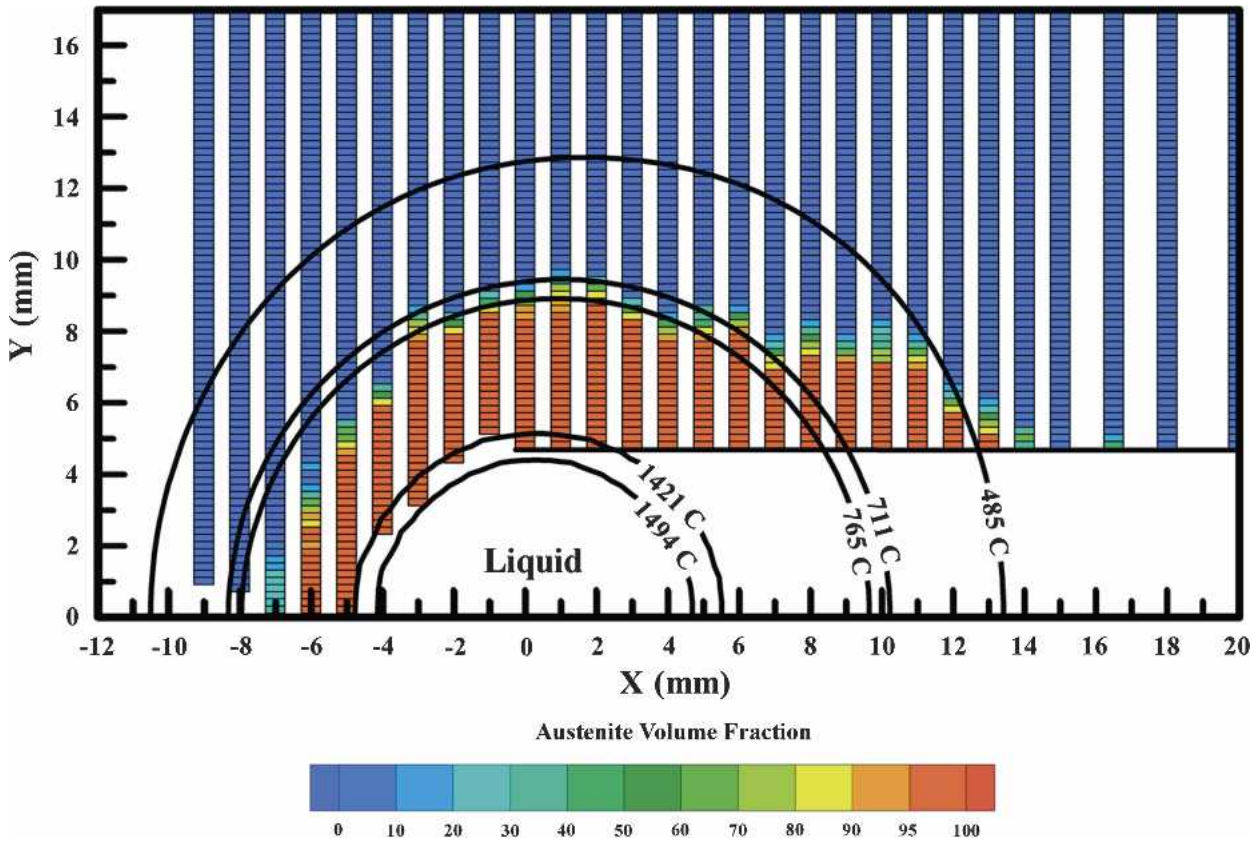

Fig. 6—SRXRD map showing the amount of austenite and ferrite existing in the HAZ of 1045 steel, overlaid with the calculated weld isotherms.

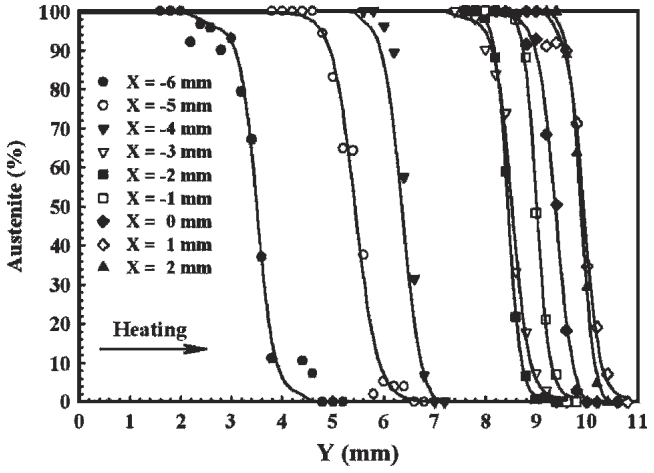

Fig. 7—SRXRD measured austenite fractions plotted *vs* weld position for the $\alpha \rightarrow \gamma$ transformation on the heating side of the weld (data points) and the best fit sigmoidal curves (lines).

Table V. Summary of the Sigmoidal Fit Parameters for the $\alpha \rightarrow \gamma$ Phase Transformation on Heating*

X (mm)	1045 Steel		1005 Steel	
	y_o	b	y_o	b
−6	3.51	−0.162	—	—
−5	5.43	−0.220	—	—
−4	6.36	−0.173	2.72	−0.305
−3	6.92	−0.164	4.24	−0.221
−2	7.84	−0.123	5.08	−0.105
−1	8.18	−0.173	5.59	−0.147
0	8.41	−0.126	6.03	−0.154
1	8.37	−0.156	6.40	−0.128
2	8.48	−0.132	6.66	−0.144
3	8.66	−0.135	7.09	−0.122

*Parameter "y_o" is the location where 50 pct of the transformation has been completed, and parameter "b" is related to the rate of transformation. Results from the 1045 steel from this study are compared to those from a previous investigation of 1005 steel.[9]

The rate of the $\alpha \rightarrow \gamma$ transformation represented by the b parameter has a value -0.157 ± 0.029 and does not change significantly with location. The relatively constant value of the b parameter indicates that the $\alpha \rightarrow \gamma$ transformation takes place at essentially the same rate over the entire leading edge of the weld HAZ.

The phase map shown in Figure 6 can also be used to determine the amount of superheat above the A3 temperature required to completely transform the microstructure to γ. Comparisons between the location of the fully transformed γ-phase field and the A3 isotherm show that the superheat varies with location, apparently due to the effect of heating rate, which increases as the weld centerline is approached. At locations close to the weld centerline, the amount of superheat is on the order of 250 °C, whereas further out ($Y > 7$ mm), the amount of superheat is approximately 50 °C or less. The results from the 1005 steel were also similar, where the average superheat above the A3

temperature was measured to be 135 °C, with a maximum value of approximately 250 °C close to the centerline of the weld.[9]

C. *The γ → α phase transformation on cooling*

The transformations that occur during weld cooling can be more complicated than those observed during heating because of the potential for the formation of nonequilibrium phases, especially at high cooling rates. It is already known that diffusion-dependant transformations such as the formation of pearlite occur at low cooling rates.[3] As the cooling rate increases, diffusion of carbon may not be rapid enough to allow the lamellar pearlite microstructure to form, and shear-type transformations become more prominent, leading to the formation of nonequilibrium phases. Bainite is one constituent that can form at these higher cooling rates. It forms through a combination of diffusion and shear at temperatures above the martensite start temperature[3] and is characterized by a microstructure of mixed ferrite and cementite with nonlamellar features. Martensite is the other nonequilibrium constituent that forms in steels at high rates and does so entirely by a shear mechanism. The martensitic microstructure contains lath- or platelike characteristics with the carbon trapped in interstitial sites of the crystal lattice.[3]

The formation of bainite and martensite cannot be described by the equilibrium phase diagram presented in Figure 3. However, calculated continuous cooling transformation (CCT) diagrams provide valuable information about microstructural evolution during weld cooling. In a previous study,[5] the model developed by Bhadeshia *et al.*[22,23] was used to predict the CCT diagram for the AISI 1045 steel. The results showed that a cooling rate faster than 10 °C/s is required to initiate bainite formation. Moreover, a cooling rate in excess of 60 °C/s is required to initiate the formation of martensite. The bainite start temperature for this 1045 steel was calculated to be 485 °C, and the martensite start temperature was calculated to be 324 °C. Both of these temperatures are far below the equilibrium A1 temperature, thus requiring significant undercooling prior to the formation of bainite or martensite.

In the TRXRD experiments performed in the previous study on 1045 steel,[5] the cooling rates were well in excess of 100 °C/s and therefore produced a predominantly martensitic microstructure. In the SRXRD welding experiments described here, significant amounts of martensite are not expected, based on the thermal profiles shown in Figure 5. These results showed that near the fusion line ($Y = 5$ mm), the heating and cooling rates peaked at approximately 80°C/s and 60 °C/s, respectively, thus precluding the formation of martensite. At HAZ locations further removed from the weld centerline ($Y = 10$ mm), the heating rate at the A1 temperature was approximately 25 °C/s, while the cooling rate was approximately 15 °C/s. Therefore, the formation of bainite is likely to occur in the HAZ of these welds, but only in the region of the HAZ closest to the fusion line where the cooling rates are the highest. Pearlite would be expected to form further out from the centerline of the weld where the cooling rates are lower.

The resulting microstructure in the HAZ of the 1045 steel weld is thus controlled by two different mechanisms as a result of the variation in cooling rates in the HAZ. The likelihood of two different $\gamma \rightarrow \alpha$ transformation mechanisms is confirmed by the SRXRD results shown in Figure 6. This phase map shows that the $\gamma \rightarrow \alpha$ transformation deviates significantly from the curvature of the A3 isotherms for HAZ locations between the fusion line and $Y = 7$ mm, where the indicated transformation temperature is significantly below the A3, and that the $\gamma \rightarrow \alpha$ transformation begins at a temperature close to the bainite start of 485 °C. The calculated weld isotherms superimposed on the SRXRD data in Figure 6 provide further evidence for the formation of bainite adjacent to the fusion line. This bainite start temperature isotherm coincides with the $\gamma \rightarrow \alpha$ transformation along the trailing side of the weld. Thus, the SRXRD data mapping of the HAZ confirms the transformation of γ into both pearlitic and bainitic regions and indicates where these transformations take place relative to the fusion line of the weld.

Optical metallography was performed on the as-welded 1045 steel sample to compare the microstructures formed in the two different regions of the HAZ. Figure 8(a) shows the

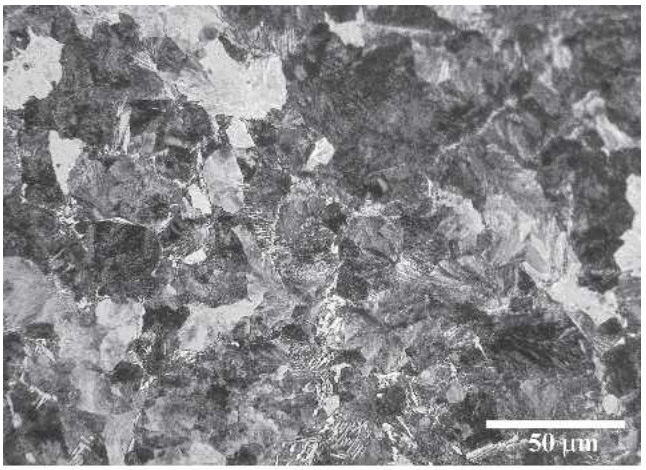

(*a*)

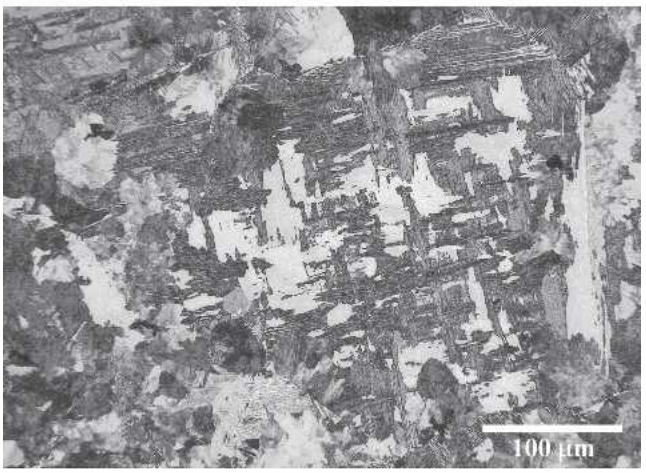

(*b*)

Fig. 8—Postweld metallographic characterization of the weld HAZ showing pearlite formation (top) in the fine-grained region of the HAZ and bainite formation in the coarse-grained region of the HAZ just adjacent to the fusion line.

microstructure near the HAZ/base metal boundary ($Y = 8$ mm) that was fully austenitized during heating. This post-weld microstructure consists of fine grains having an average diameter of approximately 20 μm, which is smaller than those of the base metal microstructure. The fine-grained microstructure of this portion of the HAZ is largely pearlitic with a small lamellar spacing. The fine grains form as a result of numerous nucleation sites within the original pearlitic microstructure (Figure 4), coupled with insufficient time for grain growth to occur. During cooling, the relatively low cooling rates and small γ grain size allowed the $\gamma \rightarrow \alpha$ transformation to occur through the reformation of pearlite.

Figure 8(b) shows the HAZ near the fusion line, which has a significantly different microstructure than that shown in Figure 8(a). In this microstructure, the prior γ grains are visible and are lightly outlined by allotriomorphic ferrite. These grains have an average diameter greater than 100 μm, which results from the high peak temperatures that approach the melting point of the alloy in this region of the HAZ. The transformed microstructure in this region of the HAZ is characteristic of bainite, having a lath-type appearance forming along multiple crystallographic variants.

D. *Splitting of Austenite Peaks*

Previous *in-situ* SRXRD X-ray observations have shown that the γ phase can exist with two different lattice parameters in this steel during weld heating, which results in a measurable splitting of the SRXRD austenite diffraction peaks.[14,15] The splitting was attributed to the presence of two types of austenite: a low-carbon austenite, which is believed to form from allotriomorphic ferrite; and a high-carbon austenite, which is believed to form from the pearlitic regions of the starting microstructure. During welding, these two types of austenite appeared at different stages of the weld thermal cycles, but eventually combined into one diffraction peak with one lattice parameter as the C and Mn diffused and redistributed into one homogeneous austenite phase at high temperatures.

This same type of splitting of the austenite peaks was observed in this study. Figure 9(a) shows an fcc(111) peak obtained at an HAZ location close to the weld fusion line where only a single austenite peak was observed ($X = 0$, $Y = 5.0$). Figure 9(b) shows a diffraction pattern obtained from the same SRXRD scan at a location further removed from the weld centerline ($X = 0$, $Y = 5.8$), where peak splitting was observed. This type of splitting was observed in all of the X-ray scans that passed through the completely austenitized region of the HAZ in this study.

A summary of the regions where austenite peak splitting is observed in each SRXRD scan is shown in Figure 10. In this plot, the start and end points of the peak split region are shown for each of the SRXRD scans through the HAZ. The triangular symbols represent the boundary where the split peak is first observed, and the square symbols represent the boundary where the peaks completely merge at higher temperatures. During weld heating, the peak splitting is first observed at locations very close to the point when the microstructure has been completely transformed to austenite at temperatures above the A3 temperature. This plot indicates that the first occurrence of peak splitting occurs

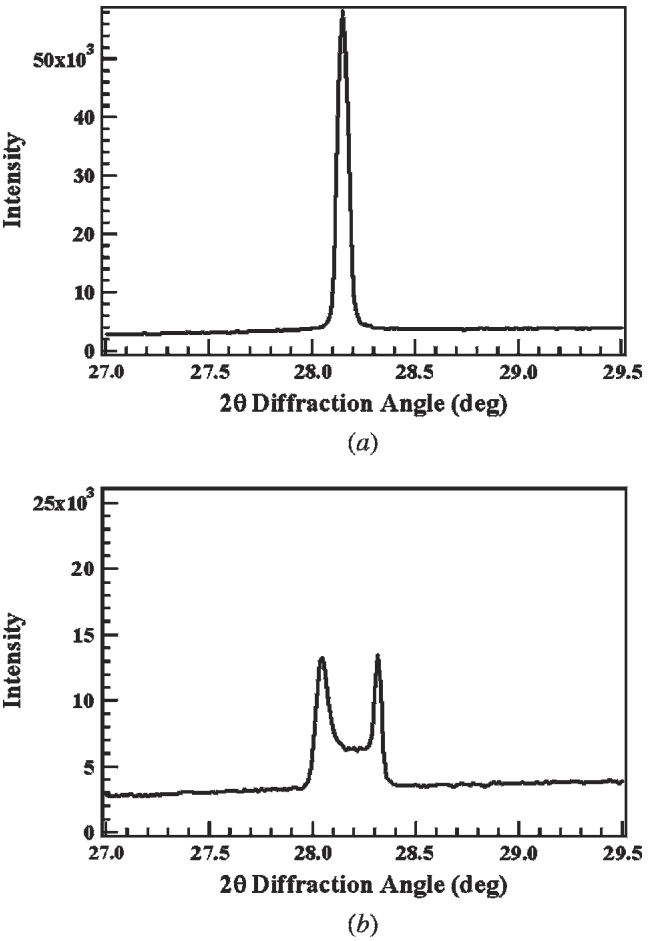

Fig. 9—XRD patterns taken at the $X = 0$ mm location showing (*a*) an fcc(111) peak located at $Y = 5.0$ mm and (*b*) splitting of the fcc(111) peak at $Y = 5.8$ mm.

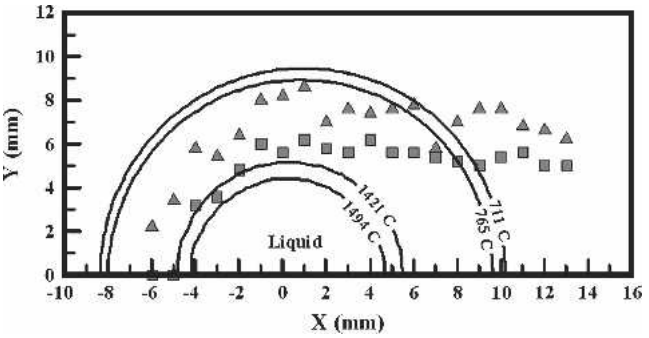

Fig. 10—Weld map showing peak split regions compared to A1 and A3 isotherms. The triangles represent the location where splitting was first observed during heating, while the squares represent the location where the split peaks combine to form a single peak.

at similar temperatures within the HAZ, since the trend of the data roughly parallels the isotherms on the heating side of the weld. The location of the HAZ where the split peaks combine to form a single peak during heating occurs at temperatures around 1400 °C, which is near the solidus temperature of this steel. During weld cooling, the peak split region is observed to continue to be present until the austenite back transforms to ferrite behind the weld.

E. *Comparison of 1045 and 1005 HAZ Transformation Kinetics*

The results from the previous SRXRD study that mapped the γ and α phase fields of the steel containing 0.05 wt pct carbon[5] can be compared to the results from this study on 0.46 wt pct carbon steel. The phase map for the low-carbon steel weld showed that the $\alpha \rightarrow \gamma$ transformation on the heating side of the weld is similar to that of the medium carbon steel. In each case, the $\alpha \rightarrow \gamma$ transformation follows the A1 temperatures on the heating side of the weld and complete transformation to γ is not observed until the temperatures exceed the A3. In both steels, the average superheating required to complete the $\alpha \rightarrow \gamma$ transformation follows similar trends, whereby the superheat increases with increasing heating rate closer to the centerline of the weld. Also, in both steels, the $\alpha + \gamma$ region was shown to exist in a band approximately 1 to 1.5 mm wide that roughly parallels the A1 and A3 isotherms up to the point where the cooling transformation begins.

Using the semiquantitative data for the $\alpha \rightarrow \gamma$ phase transformation for the 1005 steel,[9] each SRXRD data trace was also fit to the sigmoidal relationship of Eq. [1]. The fitting parameters y_o and b were then determined and are plotted in Figure 11 along with those for the 1045 steel. It is clear from this figure that the transformation rate, which is related to b, is similar for both steels and does not change significantly with weld location. The average values of this parameter are $b = -0.157 \pm 0.029$ for the 1045 steel and $b = -0.175 \pm 0.061$ for the 1005 steel, where the standard deviation is indicated. The slightly more negative value for the 1005 steel indicates that this transformation is faster and takes place over a slightly narrower range than for the 1045 steel. The larger difference in Figure 11 is the comparison between the y_o values for the two different steels, which are related to the distance from the centerline of the weld where the transformation takes place. The larger y_o values for the 1045 steel indicate that the $\alpha \rightarrow \gamma$ transformation is taking place further from the centerline of the weld than for the 1005 steel. One reason for this is that the welding parameters used in the two SRXRD studies were not identical, with those used in the 1045 steel welds being approximately 20 pct higher in power than those used in the 1005 steel welds. The different heat inputs were required from the different fluid flow characteristics of each steel. The 1045 steel, with higher sulfur content, required a higher heat input than the 1005 steel to produce a similar weld pool width.

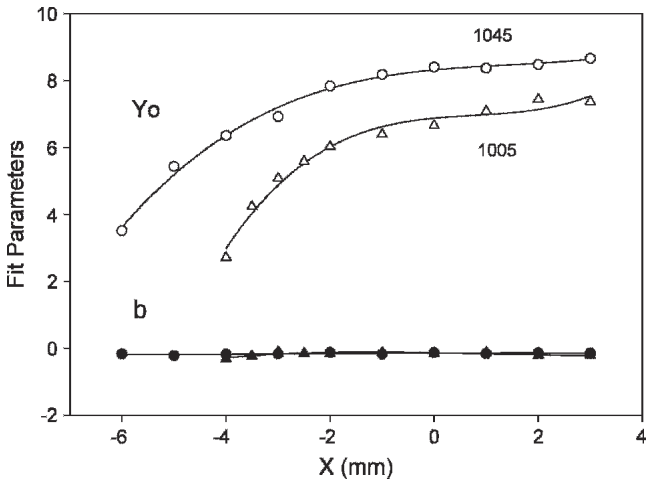

Fig. 11—Sigmoidal fit parameters for the $\alpha \rightarrow \gamma$ transformation from the SRXRD data at different x-axis locations along the weld. The parameter y_o (open symbols) represents the location where 50 pct of the $\alpha \rightarrow \gamma$ transformation had taken place, and the b parameter (solid symbols) represents the rate of transformation. Data for both the 1045 steel (circles) and 1005 steel (triangles) are compared.

Even with the different heat inputs, the two steels display similar transformation characteristics during heating. For example, both show a band of $\alpha + \gamma$ coexistence of approximately 1- to 1.5-mm wide that roughly parallels the A1 and A3 isotherms, but is displaced behind these isotherms, indicating that superheating is required to initiate and complete the $\alpha \rightarrow \gamma$ transformation. The location of the 50 pct transformation line, indicated by y_o, lies just above the A3 isotherm for both steels, and the transformation rate, as indicated by b, indicates that the range where both phases coexist is slightly larger for the higher sulfur content 1045 steel.

During weld cooling, the 1005 and 1045 steels behave differently. In the 1005 steel,[9] the $\gamma \rightarrow \alpha$ transformation parallels the A1 isotherm, wrapping around the back side of the weld. Throughout the entire HAZ, this transformation was largely complete when the A1 temperature was reached, which would be expected for transformation *via* a nucleation and growth mechanism. In contrast, the 1045 steel displays two different transformation mechanisms on cooling. For the fine-grained region of the HAZ farther from the weld fusion line, the transformation is similar to that of the 1005 steel, where the transformation is largely complete when the A1 temperature is reached. However, for regions closer to the fusion line, in the large-grained region of the HAZ, the $\gamma \rightarrow \alpha$ transformation of the 1045 steel required significantly higher undercoolings to complete the transformation. These large undercoolings are associated with the formation of bainite, which begins to form from γ at 485 °C and was confirmed through postweld optical metallographic characterization.

IV. CONCLUSIONS

1. *In-situ* SRXRD experiments were used to map the phases present in the HAZ during GTA welding of AISI 1045 steel, while a 3-D coupled thermal fluids model was used to calculate both the shape of the liquid weld pool and the temperature distribution in the HAZ. The resulting map plots the phases present around the HAZ during welding with submillimeter precision and compares the phase fields with the phase transformation isotherms. The results show a relatively large austenite field, reaching 3 mm in width, and the evolution of this phase field during weld heating and cooling.
2. A comparison of the SRXRD measured location of the single-phase austenite region with the calculated A3 temperatures for this steel shows that the amount of superheat required to complete the $\alpha \rightarrow \gamma$ phase transformation during weld heating increases with heating rate. Superheating as high as 250 °C above the A3

temperature was observed in the region of the HAZ with the highest heating rate of 80 °C/s.

3. During weld heating, γ was observed to exist with two different lattice constants that resulted in a splitting of the γ diffraction peaks. The peak splitting appears to be caused by the formation of low-carbon/manganese and high-carbon/manganese constituents due to the inhomogeneous starting microstructure that consists of allotriomorphic ferrite and higher C/Mn pearlite. These two austenite constituents homogenize to form austenite with a single lattice parameter in the high-temperature regions of the HAZ that are located close to the weld fusion line.
4. Two different $\gamma \rightarrow \alpha$ phase transformation behaviors were observed during weld cooling. In the fine-grained region of the HAZ at distances greater than approximately 2 mm from the fusion line, the transformation reached completion at temperatures close to the A1 temperature with only small amounts of undercooling. For distances within 2 mm of the fusion line, the $\gamma \rightarrow \alpha$ transformation occurred with undercoolings on the order of 200 °C below the A1 temperature. This difference in transformation behavior corresponds to nucleation and growth of pearlite at locations far from the fusion line, and the formation of bainite closer to the fusion line where the grains are larger and the cooling rates are higher.
5. The kinetics of the $\alpha \rightarrow \gamma$ transformation in the 1045 steel were compared to those of the 1005 steel that was previously mapped using the SRXRD technique.[9] During heating, both steels behaved similarly, requiring similar superheating above the A3 temperature to complete the $\alpha \rightarrow \gamma$ transformation. During cooling, the 1005 steel completed the $\gamma \rightarrow \alpha$ transformation near its A1 temperature for all regions of the HAZ. However, the 1045 steel showed a deviation from this trend close to the fusion line where the bainitic transformation was observed at temperatures significantly lower than the A1 temperature.

ACKNOWLEDGMENTS

This work was performed under the auspices of the United States Department of Energy, Lawrence Livermore National Laboratory, under Contract No. W-7405-ENG-48. Portions of this work were supported by the DOE, Office of Basic Energy Sciences, Division of Materials Science. The synchrotron aspects of this research were carried out at the Stanford Synchrotron Radiation Laboratory, a national user facility operated by Stanford University on behalf of the United States Department of Energy, Office of Basic Energy Sciences. The authors express their gratitude to Mr. Bob Vallier, LLNL, for performing the metallographic characterization of the base metal and welded samples.

REFERENCES

1. Ø. Grong: *Metallurgical Modelling of Welding*, The Institute of Materials, London, 1994, ch. 1.
2. M.F. Ashby and K.E. Easterling: *Acta Metall.*, 1982, vol. 30, pp. 1969-78.
3. J.C. Ion, K.E. Easterling, and M.F. Ashby: *Acta Metall.*, 1984, vol. 32, pp. 1949-62.
4. G.S. Huppi, D.K. Matlock, and G. Krauss: *Scripta Metall.*, 1980, vol. 14, pp. 1239-43.
5. J.W. Elmer, T.A. Palmer, S.S. Babu, W. Zhang, and T. DebRoy: *Welding J.*, 2004, vol. 83 (9), pp. 244-s-253-s.
6. J. Wong, T. Ressler, and J.W. Elmer: *J. Synchrotron Radiation*, 2003, vol. 10, Part 2, pp. 154-67.
7. W. Zhang, G.G. Roy, J.W. Elmer, and T. DebRoy: *J. Appl. Phys.*, 2003, vol. 93 (5), pp. 3022-33.
8. J.W. Elmer, J. Wong, and T. Ressler: *Metall. Mater. Trans. A*, 2001, vol. 32A, pp. 1175-87.
9. J.W. Elmer, T.A. Palmer, W. Zhang, B. Wood, and T. DebRoy: *Acta Mater.*, 2003, vol. 51, pp. 3333-49.
10. W. Zhang, J.W. Elmer, and T. DebRoy: *Sci. Technol. Welding Joining*, 2005, vol. 10 (5), pp. 574-82.
11. W. Zhang, J.W. Elmer, and T. DebRoy: *Scripta Mater.*, 2002, vol. 46, pp. 753-57.
12. W. Zhang, J.W. Elmer, and T. DebRoy: *Mater. Sci. Eng., A*, 2002, vol. 333 (1–2), pp. 320-35.
13. A. Kumar, S. Mishra, J.W. Elmer, and T. DebRoy: *Metall. Mater. Trans. A*, 2005, vol. 36A, pp. 15-22.
14. T.A. Palmer and J.W. Elmer: *Scripta Mater.*, 2005, vol. 53 (5), pp. 535-40.
15. T.A. Palmer and J.W. Elmer: *Metall. Mater. Trans. A*, 2005, vol. 36A, pp. 3353-69.
16. S. Babu: Oak Ridge National Laboratory, Oak Ridge, TN, private communication, 2002.
17. B. Sundman, B. Jansson, and J. Andersson: *CALPHAD*, 1985, vol. 9 (2), pp. 153-90.
18. K. Mundra, T. DebRoy, and K. Kelkar: *Num. Heat Transfer*, 1996, vol. 29, pp. 115-29.
19. Z. Yang and T. DebRoy: *Metall. Mater. Trans. B*, 1999, vol. 30B, pp. 483-93.
20. M.W. Chase, Jr., C.A. Davies, J.R. Downey, Jr., D.J. Frurip, R.A. McDonald, and A.N. Syverud: *JANAF Thermochemical Tables*, 3rd ed., American Chemical Society and American institute for Physics, Washington, DC, 1985.
21. *Smithells Metals Reference Book*, 7th ed., E.A. Brandes, ed., Butterworth and Heinemann, London, 1992.
22. H.K.D.H. Bhadeshia, L.E. Svensson, and B. Gretoft: *Acta Metall.*, 1985, vol. 33 (7), pp. 1271-83.
23. H.K.D.H. Bhadeshia: *Met. Sci.*, 1982, vol. 16 (3), pp. 159-65.